Journal of Alloys and Compounds 769 (2018) 1007–1018

Contents lists available at ScienceDirect

Journal of Alloys and Compounds

journal homepage: http://www.elsevier.com/locate/jalcom

In-situ gas reduction in reversible SnS-SnO_2@N-doped graphene anodes for high-rate and lasting lithium storage

Mengjiao Li [a], Qinglin Deng [a], Junyong Wang [a], Kai Jiang [a, **], Liyan Shang [a], Zhigao Hu [a, b, *], Junhao Chu [a]

[a] Key Laboratory of Polar Materials and Devices (MOE) and Technical Center for Multifunctional Magneto-Optical Spectroscopy (Shanghai), Department of Electronic Engineering, East China Normal University, Shanghai 200241, China
[b] Collaborative Innovation Center of Extreme Optics, Shanxi University, Taiyuan, Shanxi 030006, China

ARTICLE INFO

Article history:
Received 22 May 2018
Received in revised form
3 August 2018
Accepted 4 August 2018
Available online 10 August 2018

Keywords:
SnO_2
SnS
Graphene
Lithium ion battery
Heterostructures

ABSTRACT

Ameliorating the conductivity and terrible phase aggregation are the primary tasks of tin-based anodes for practical applications in lithium storage. Inspired by this, we have adopted an in-situ gas reduction strategy for fine SnS-SnO_2 nanoparticles anchoring uniformly on N-doped graphene (C@SnS-SnO_2@NGr) to realize superior rate performance in lithium-ion batteries (LIBs) applications. Especially, the better electric contact between SnS and SnO_2 can avoid localized reaction of SnM_x (M signifies O/S) and retard serious aggregation of Sn/Li_xSn. As a result, a higher initial Coulombic efficiency (ICE) (78%) was achieved with almost reversible conversion reaction of Sn/Li_2M. The capacity retention reaches around 85% at the current density of 0.1 A g^{-1} for 500 cycles (1120 mA h g^{-1}). Besides, the N-doped graphene as the skeleton benefits the well-distribution of p-n SnS-SnO_2 nanoparticles and the conductivity of hybrids. Through high-rate and longest evaluation of 2.0 A g^{-1}, the unique anode still keeps a high capacity of 630 mA h g^{-1} above 1000 cycles, which accordingly reveals a dominated surface-controlled redox reaction. Correspondingly, the evolution of electrode indicates that the ameliorate conductivity by N-doped graphene and the in-situ gas reduction procedure indeed enhance the charge-transfer kinetics and contribute to a durable high-rate performance.

1. Introduction

With the wide application of flexible electronic equipment, the growing demands for rechargeable lithium ion batteries (LIBs) with high capacity and reliability cannot be met from conventional graphite anodes. Under this background, the homology-based semiconductors (Si/Sn) with higher theoretical capacity and abundance performs as an ideal candidates [1–4]. Hence, more specific researches of anodes materials have been gradually concentrated on transition metal oxides and chalcogenides considering the conversion and alloying reaction process [5–11]. SnO_2 is known for its low cost and almost twofold storage ability of lithium compared with currently used graphite. Initially, during the irreversibly conversion process Eq.(α) $SnO_2 + 4Li^+ + 4e^- \rightarrow Sn + 2Li_2O$, Li_2O groups act as a reliable cushion for mechanical stress and grievous volume expansion to some extents. In the subsequent Li alloying reaction Eq. (β) $Sn + xLi^+ + xe^- \rightarrow Li_xSn$, the weak electrical contact between Sn-Li_xSn and Li_2O brings about distinct aggregation [12–15]. Unfortunately, these bigger particles will suffer the cracking from internal strain, resulting in limiting the transportation of ions/electrons, which brought worse stability and rate performance of SnO_2 anodes [16,17].

Recently, many efforts have been made to improve the reliability performance of SnO_2-based anodes, which mainly focused on how to provide conductive matrix and how to build a novel tough structure. Apart from choosing carbon-based matrix to improve conductivity, moreover, charge-transfer kinetic can be enhanced by constructing a rational heterostructure with built-in driving force [18–25]. For instance, the tunable charge inversion-depletion layer between MoS_2-WSe_2 has been investigated systematically in virtue

* Corresponding author. Key Laboratory of Polar Materials and Devices (MOE) and Technical Center for Multifunctional Magneto-Optical Spectroscopy (Shanghai), Department of Electronic Engineering, East China Normal University, Shanghai 200241, China.
** Corresponding author.
E-mail addresses: kjiang@ee.ecnu.edu.cn (K. Jiang), zghu@ee.ecnu.edu.cn (Z. Hu).

https://doi.org/10.1016/j.jallcom.2018.08.038
0925-8388/

of photocurrent tests, which proves the advantages of hetero-interface interaction [26]. According to the band structure, SnS is a suitable partner of internal encouraged kinetics to form a p-n junction with SnO_2. Specifically, SnS has a better conductivity than SnO_2 relying on more covalent metal-sulfur bonds. Stacked layered structure contributes to the storage of Li^+ and accordingly endows SnS with a higher initial Coulombic efficiency and reversibility [21,27–31]. Several studies of SnS or SnO_2-based composites have been applied to photocatalysis, energy storage or electronic devices, via hydrothermal or liquid phase transfer methods [5,8,22,25,32–35]. However, the controlling of homogeneous heterointerfaces has been ignored under normal conditions, which is of vital significance for better carriers transfer and surface reactions. Therefore, further efforts should focus on how to completely develop the synergistic effects of ultra-fine hetero-interface for Li^+ storage materials.

Motivated by improved conductivity and superior heterointerface, the SnS-SnO_2 nanoparticles anchoring on N-doped graphene (C@SnS-SnO_2@NGr) has been employed to obtain expected durable storage of Li^+. Especially, the uniformity of weeny SnS-SnO_2 heterostructure is ensured from a free H_2S gas reduction strategy. The internal charge-transfer force promotes the ion/electron diffusion and avoid localized reaction of SnM_x (O/S) to Li_2M. Superior electric contact and better synergistic effect among SnS/SnO_2 and graphene matrix can effectively subdue the serious aggregation of Sn/Li_xSn. Therefore, the expected reversible conversion between SnM_x and Sn/Li_2M contributes to a higher ICE (78%), up 26% than that of SnO_2@Gr. Based on the dominated surface-controlled capacity reaction, the novel electrode delivers an excellent rate performance with the reversible capacity of 630 mA h g^{-1} for 2000 cycles (2.0 A g^{-1}). Such active and durable anode with pseudocapacitive kinetics may make a paradigm to alloying-anodes in enhancing the storage performance.

2. Experimental details

2.1. Preparation of pre-S-SnO_2@NGr

First, colloidal H_2SnO_3 precursor was prepared by a simple hydrothermal method. 1 mmol $SnCl_4 \cdot 5H_2O$ was dissolved in 40 mL deionized (DI) water, and transferred into a 50 mL Teflon-lined stainless steel autoclave at 180 °C for 15 h. After cooled down to room temperature, the milky resultant was collected and washed with DI water several times. Then the precursor was mixed with 5 mL graphene oxide (GO) solution (3 mg mL^{-1}) under strong magnetic stirring for 2 h, following added 50 mg thioacetamide (TAA). In order to get a homogeneous distribution and sulfuration of SnO_2 nanoparticles, the adequate mixture and hydrothermal treatment at 150 °C are essential. Note that the GO was prepared with a modified Hummer's method and the TAA acts as both the nitrogen and sulfur supplier [36]. Then the collected products was washed with DI water and freeze-dried (Pre-S-SnO_2@NGr).

2.2. Preparation of SnS-SnO_2@NGr and C@SnS-SnO_2@NGr

Then the gas reduction process was completed by an anneal treatment under argon at 500 °C for 3 h. During the annealing, not only the GO can be reduced, but the sulfur (HS-/S-) groups attached on Pre-S-SnO_2@NGr also can produce H_2S reduction gas. Thus, through a simple gas reduction, the SnO_2/SnS heterostructure can be obtained uniformly (SnS-SnO_2@NGr). Then, an advanced facile method to coat an uniform carbon film outside the aerogel has been adopted through phase polymerization and carbonization. In detail, the as-synthesized SnS-SnO_2@NGr was put into the upstream of a sealed 500 ml beaker prefilled with pyrrole at 80 °C for forming a thin polypyrrole film. Finally, the above sample encapsulated with carbon layer can be prepared through a carbonization treatment at 400 °C for 3 h with the argon (C@SnS-SnO_2@NGr).

2.3. Preparation of SnO_2@Gr and SnS@Gr

Generally, SnO_2@Gr could be obtained with the same method as Pre-SnS-SnO_2@NGr, apart from adding TAA. Likewise, SnS@Gr was prepared with 1 mmol $SnCl_2 \cdot 2H_2O$, thiourea, and GO solution in ethylene glycol.

2.4. Characterization methods

X-ray diffraction (XRD) was used to characterized the crystallinity and purity of the as-prepared samples (Bruker D8 Advance diffractometer, equipped with Cu Kα radiation). Raman spectroscopy and X-ray photoelectron spectroscopy (XPS) analysis were conducted by Jobin-Yvon LabRAM HR 800 micro-Raman spectrometer and RBD upgraded PHI-5000C ESCA system, respectively. For exploring the morphological features of the samples, Field emission scanning electron microscopy (FESEM, JEOL-JSM-6700F) and transmission electron microscopy (TEM) were employed, as well as the high resolution transmission electron microscopy (HRTEM) and elemental mappings studies. In addition, the specific surface area were calculated by the Brunauer-Emmett-Teller (BET) method (TriStar II 3020, America). The thermogravimetric analysis (TGA, TA Instruments 2000) were performed in air from 60 to 800 °C in air (10 °C min^{-1}).

2.5. Lithium ion batteries tests

To investigate the LIB applications, the anodes were prepared by mixing the as-prepared samples (80%), acetylene black (10%), and poly(vinyl-difluoride) (PVDF) (10%) in N-methy-2-pyrrolidone (NMP) for a slurry. The mass of each electrode with a diameter of 12 mm were about 0.8 mg cm^{-2} and 2.5 mg cm^{-2} for comparison. For assembling and tests, the Celgard 2400 membrane and Li foils were used as the separator and counter electrode, respectively. The electrolyte was 1 M $LiPF_6$ in ethylene carbonate/dimethyl carbonate/ethyl methyl carbonate with the volume ratio of 1:1:1. In detail, galvanostatic cycling tests were conducted by the Land Battery-Testing station with the voltage range of 0.02–3.0 V (vs. Li^+/Li). The Cyclic voltammograms (CV) curves were recorded at the scan rate of 0.5 mV s^{-1} by a CHI660E electrochemical workstation. The electrochemical impedance spectroscopy (EIS) was also measured in the frequency range of 0.01–100 k Hz.

3. Results and discussion

3.1. Fabrication procedure of integrated composite

Fig. 1 presents the gas reduction fabrication procedure of the carbon sealed SnS-SnO_2 nanoparticles anchoring on N-doped graphene (C@SnS-SnO_2@NGr). Firstly, in order to acquire well-dispersed particles, a hydrothermal process for colloidal H_2SnO_3 precursor has been adopted instead of crystalline SnO_2 powder. Then, owing to the presence of functional groups, GO forms a favorable dispersion in DI water with H_2SnO_3 precursor and TAA, which are the origin of H_2S gas. After the thermal treatment, SnO_2 particles are entirely packaged in shrink graphene aerogel. At the same time, TAA, acting as both the nitrogen and sulfur supplier, liberates sulfur (HS-/S-) and nitrogenous groups for the precursor. Thus, a pre-sulfuration treatment endows SnO_2-Gr aerogel the wholly-distributed sulfur-groups, meanwhile extra nitrogen-doped (N-doped) induced defect sites for more lithium storage.

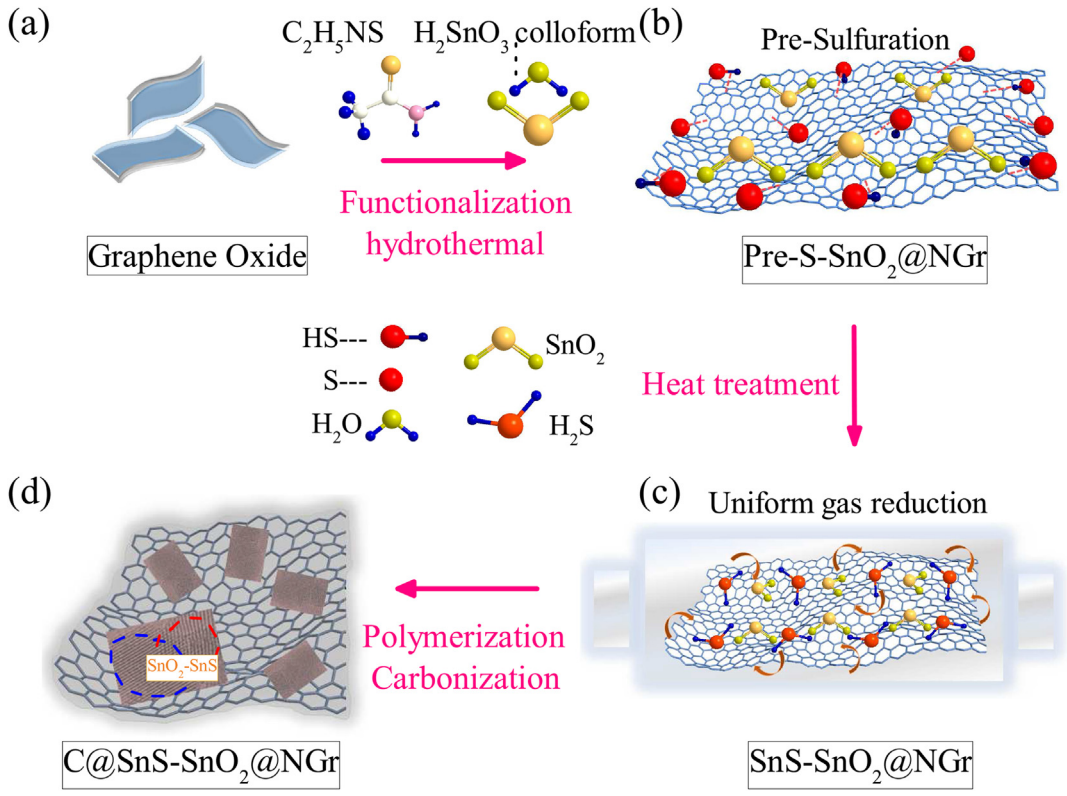

Fig. 1. Schematic illustration of the fabrication procedure of the integrated C@SnS-SnO_2@NGr composite. (a)–(b) The hydrothermal and pre-sulfuration process of Pre-S-SnO_2@NGr based on graphene aerogel. (c)–(d) The gas reduction, vapor polymerization, and carbonization treatment for preparing carbon-sealed uniform fine SnO_2/SnS nanoparticles anchored on N-doped graphene

Subsequently, during the heating reduction, the production of H_2S gas derived from sulfur-groups diffuses to SnO_2 particles, which forming the SnS-SnO_2 heterostructure. Finally, a uniform carbon layer has been achieved through vapor phase polymerization and carbonization process to endow the structural integrity during the galvanostatic discharge-charge process. It is worth mentioning that the pre-sulfuration and gas reduction strategy brought fine and well-distributed SnS-SnO_2 nanoparticles [37]. Therefore the localized reaction of SnM_x (O/S) to Li_2M and serious aggregation of Sn/Li_xSn can be effectively avoided during cycle reactions.

3.2. Morphology analysis

Fig. 2 shows the morphologies of the as-synthesized SnO_2 nanoparticles decorated graphene and the hybrids from gas reduction by scanning electron microscopy (SEM) and transmission electron microscopy (TEM). Before sulfuration, as shown in Fig. 2b, lots of SnO_2 nanoparticles evenly anchored on graphene sheets, which indicates that colloidal H_2SnO_3 benefits the dispersion of SnO_2-H_2O particles on graphene. In addition, the HRTEM image (Fig. 2c) and inset fast Fourier transform (FFT) spots reveal parallel lattice fringes of $d = 2.58$ Å and $d = 3.29$ Å, corresponding to the (101) and (110) planes of SnO_2 crystal, respectively [38]. After gas reduction treatment, the features of C@SnS-SnO_2@NGr in Fig. 2d present high similarity with plentiful nanoparticles, especially some obvious overlaps. It can be manifested that SnS-SnO_2@NGr renders stable structure and electrochemical properties after sulfuration. Significantly, the formation of SnO_2-SnS hybrids can be affirmed by HRTEM result in Fig. 2e. Besides the existence of SnO_2 crystal planes, some others lattice fringes of $d = 2.82$ Å and $d = 3.38$ Å (inset FFT spots) can be assigned to the (301) and (201) planes of SnS crystal, respectively [39]. Accordingly, SnS and SnO_2 have an intimate contact deriving from the common Sn sources. Also, the corresponding cleaved crystal structures in Fig. S1 indicates that the distance between six adjacent Sn atoms on the (101) crystal surface of SnO_2 (0.4735 nm × 6) matches well with seven intervals of the S-S on the (301) crystal surface of SnS (0.4023 nm × 7), which endows the covalent force of the hybrids. Likewise, the distance of four Sn-Sn atoms on the (110) crystal surface of SnO_2 (0.3184 nm × 4) is agreement with three intervals of the S-S on the (210) crystal surface of SnS (0.4294 nm × 3), which acts as strong evidence for the interrelated effect between SnO_2 and SnS nanoparticles. Furthermore, the uniformity fine particles (10–12 nm) over whole samples can be ensured (Fig. S1) through the gas reduction strategy, which accelerates the ion/electron transfer and avoids the localized aggregation during the cycling reactions. Besides, in Fig. 2f, elemental mapping analysis reveals a well spatial distribution of C, Sn, S, O, and N, which demonstrate the effective sulfuration and the intimate formation of the SnS-SnO_2 hybrids.

3.3. Phase structure, Raman, XPS analysis, and evolution studies

X-ray diffraction (XRD) analysis were conducted to investigated all the phase information and purity of all the prepared samples in Fig. 3a. The diffraction peaks in patterns I and III locate at 2θ of 26.7°, 33.9°, 51.7° and 65.9° match well with (110), (101), (211), and (301) crystal faces of tetragonal rutile SnO_2 (JCPDS#41-1445), respectively [40]. The other featured peaks are related to orthorhombic SnS (JCPDS#65-3812), with characteristic peaks at 21°, 27.5°, 31.5°, 32.1°, 39.2°, and 44.7° for (101), (210), (301), (400), and (311) planes, respectively [41]. All of the characteristics can be entirely probed in pattern I, which indicates that partial SnO_2 has been

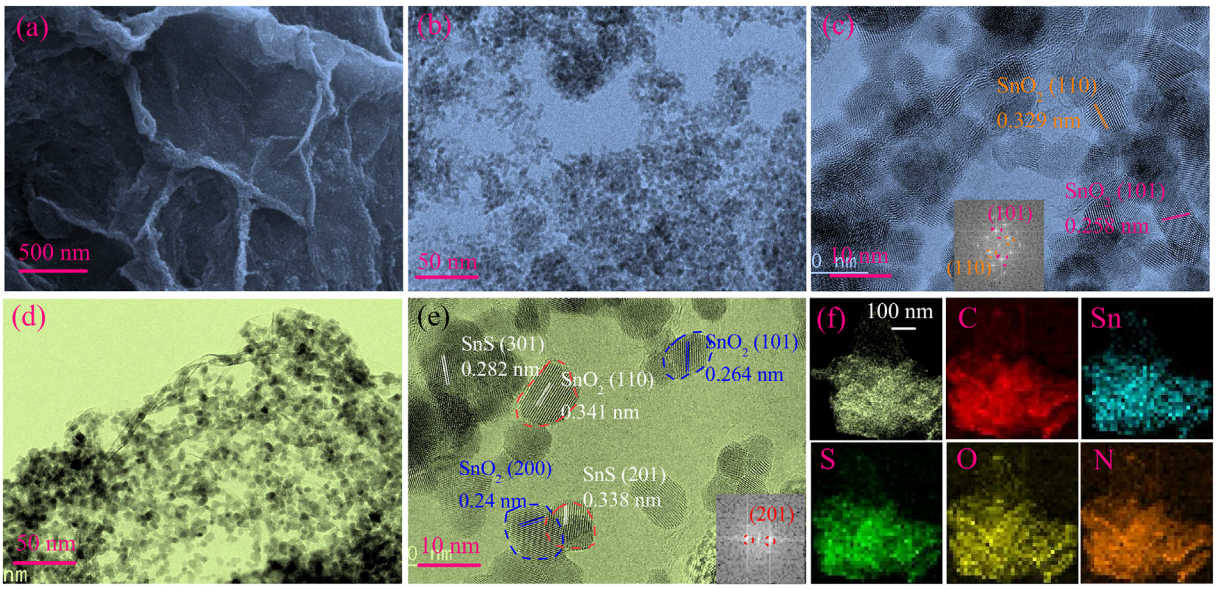

Fig. 2. (a) SEM, (b) TEM, and (c) HRTEM images of SnO_2@Gr. (d) TEM and (e) HRTEM of C@SnS-SnO_2@NGr composites. Inset (c) and (e) are the fast Fourier transform patterns for SnO_2 and SnS, respectively. (f) The corresponding TEM-element mapping images of C, Sn, S, O, and N.

reducted to SnS as expected. Besides, the analogical broadening of diffraction peaks in patterns I and II shows that the homogeneous small particles were not aggregated after sulfuration, compared with pattern II. It is agreement with the SEM and TEM results above, and the bigger granules can be found from the morphologies of SnS@Gr (Fig. S2). Raman spectroscopy at the range of 100–1800 cm^{-1} were collected with 532 nm laser. In Fig. 3b, several characteristic peaks located at around 501.6, 620.4, 683.9, and 759.2 cm^{-1} can be assigned to the A_{2u} TO, A_{1g}, A_{2u} LO, and B_{2g} vibration modes, respectively, which reflect the symmetric and asymmetric Sn-O stretching. Interestingly, another peak at around 552.3 cm^{-1} cannot be ignored, which probably derived from the local lattice disorder or oxygen vacancies, and this phenomenon can be also observed in other works [42]. A slight shift to lower wave number from pure SnO_2 to SnO_2@Gr and SnS-SnO_2@NGr has been found in Fig. S3. In especial, the featured peak at around 620.4 cm^{-1} could be correlated to internal stress between nanoparticles and GO sheets. In SnS@Gr, Raman scatting peaks positioned at 160.4, and 221.5 cm^{-1} can be detected, which become inconspicuous in the hybrids, demonstrating the decoration of SnS-SnO_2 nanoparticles on NGr and the coverage of carbon. The peaks can be attributed to B_{3g} and A_g modes of SnS, respectively [39,43]. There also exist two band (D band and G band) of graphene at 1332 and 1588 cm^{-1}. Obviously, the intensity ratio between two peaks (I_G/I_G) of the C@SnS-SnO_2@NGr (1.66) is larger than two pure phases, which may be attributed to the exfoliation structure and the insertion of SnS particles via H_2S gas reduction evenly [27,44].

Chemical states of as-prepared composites are examined by X-ray photoelectron spectroscopy (XPS) shown in Fig. 3c–d and Fig. S4. The result of C@SnS-SnO_2@Gr contains the distinctive peaks of both SnO_2@Gr and SnS@Gr, and indicates the coexistence of SnS-SnO_2 hybrids and the main presence of O, C, S, N, and Sn elements. In the C 1s spectrum (Fig. 3c), three main peaks at 284.4, 285.8, and 288.6 eV can be assigned to sp^2 C=C, C-N, and C=O, respectively [45]. From the Sn 3d profile (Fig. 3d), for SnO_2@Gr the binding energy peaks of 487.23 eV and 495.64 eV are indexed to Sn $3d_{5/2}$ and Sn $3d_{3/2}$, respectively. Notably, after sulfuration and carbon coating, Sn 3d peaks shift toward the lower binding energy. Through the fitted results of Sn 3d, four dominate peaks at 486.8 and 495.2 eV belong to Sn^{4+}, and another two peaks around 485.9 and 494.3 eV disclose the existences of Sn^{2+}, respectively. Thus we can deduce that the obvious red shift is derived from the related electronic shielding synergistic effect of Sn with different electronic states in heterostructure [24,46]. In addition, the TGA and EDS analysis have been conducted to certify the contents of C (Fig. S5) and the component of SnO_2 and SnS. In detail, from the atomic ratio of S element, the component of SnO_2 and SnS can be inferred to be around 1.75:1. The TGA curves of C@SnS-SnO_2@NGr and SnS-SnO_2@Gr shown in Fig. 3e indicate that the weight losses are about 9% and 8%, respectively. Note that there is no obvious weight change when SnS oxidizing to SnO_2, thus the weight loss should be assigned to the amount of graphene and carbon. Therefore, it indicates the existence of carbon layer, which is generated by the carbonization of polypyrrole. In especial, the carbon layer with the amount of around 1% could provide an intact protection of whole structure. This result matches well with the analysis of EDS (14.35%) and theoretical value (around 10%), taking the extra carbon adsorption and substrate in the EDS measurement into consideration. Fig. 3f presents the nitrogen adsorption-desorption isotherms and the pore-size distribution of C@SnS-SnO_2@NGr and graphene aerogel. Obviously, C@SnS-SnO_2@NGr composite owns a mesopore structure with narrow size distributions (about 4.3 nm/8.4 nm) and a sizable specific surface area of 108.9 $m^2 g^{-1}$. While the pure graphene aerogel has a bigger specific surface area of 212.6 $m^2 g^{-1}$, which is contributed to the lighter pile up and without the decorating of SnO/SnS nanoparticles. Therefore, after gas reduction, it can bring sufficient contact between electrolyte and anodes, and further provide available space to buffer the volume change to improve the electrochemical performance.

To corroborating the gas reduction methods above, contradistinctive studies with the further insight of XRD, XPS, SEM, and TEM-element mapping have been conducted. In Fig. 4a, without the addition of GO and thermal annealing process, no discernable XRD characteristic peaks of SnS could be detected in the precursor (Pre-S-SnO_2@NGr), excepting SnO_2. While, after simple annealing treatment, obvious XRD reflection of SnS occurs, along with the SnO_2 (SnO_2-SnS). Likewise, from the Sn 3d spectra of XPS results, a distinct red shift after reduction could be found (Fig. 4b), as the

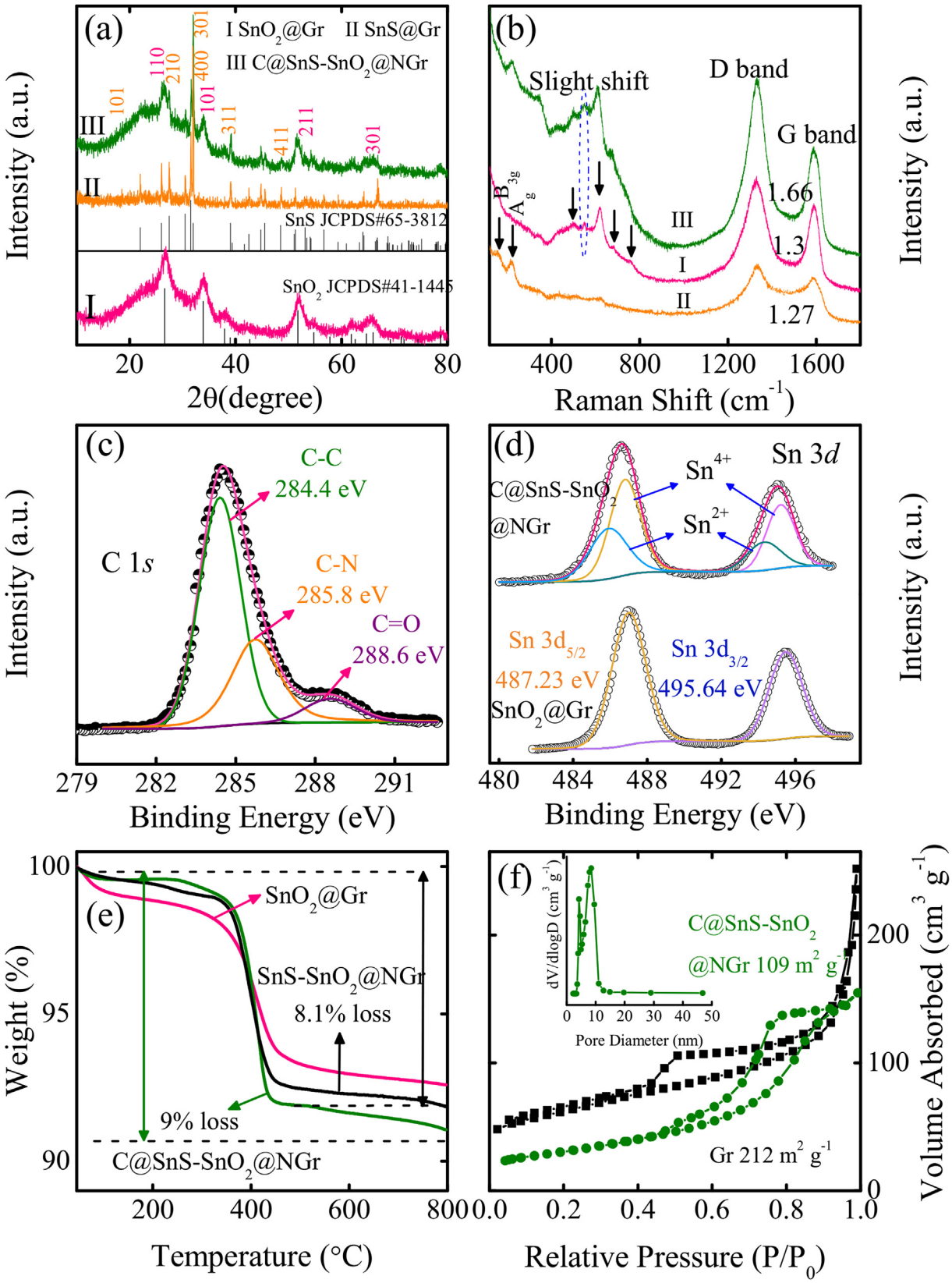

Fig. 3. (a) XRD patterns and (b) Raman spectra of as-prepared composites. The high resolutions for (c) C 1s and (d) Sn 3d of C@SnS-SnO_2@NGr and SnO_2@Gr anodes. Note that the scatter and solid lines indicate the experimental data and fitted results, respectively. (e) TGA curves of C@SnS-SnO_2@NGr, SnS-SnO_2@NGr, and SnO_2@Gr anodes. (f) Nitrogen adsorption-desorption isotherms and the pore-size distribution (inset) of C@SnS-SnO_2@NGr and graphene aerogel.

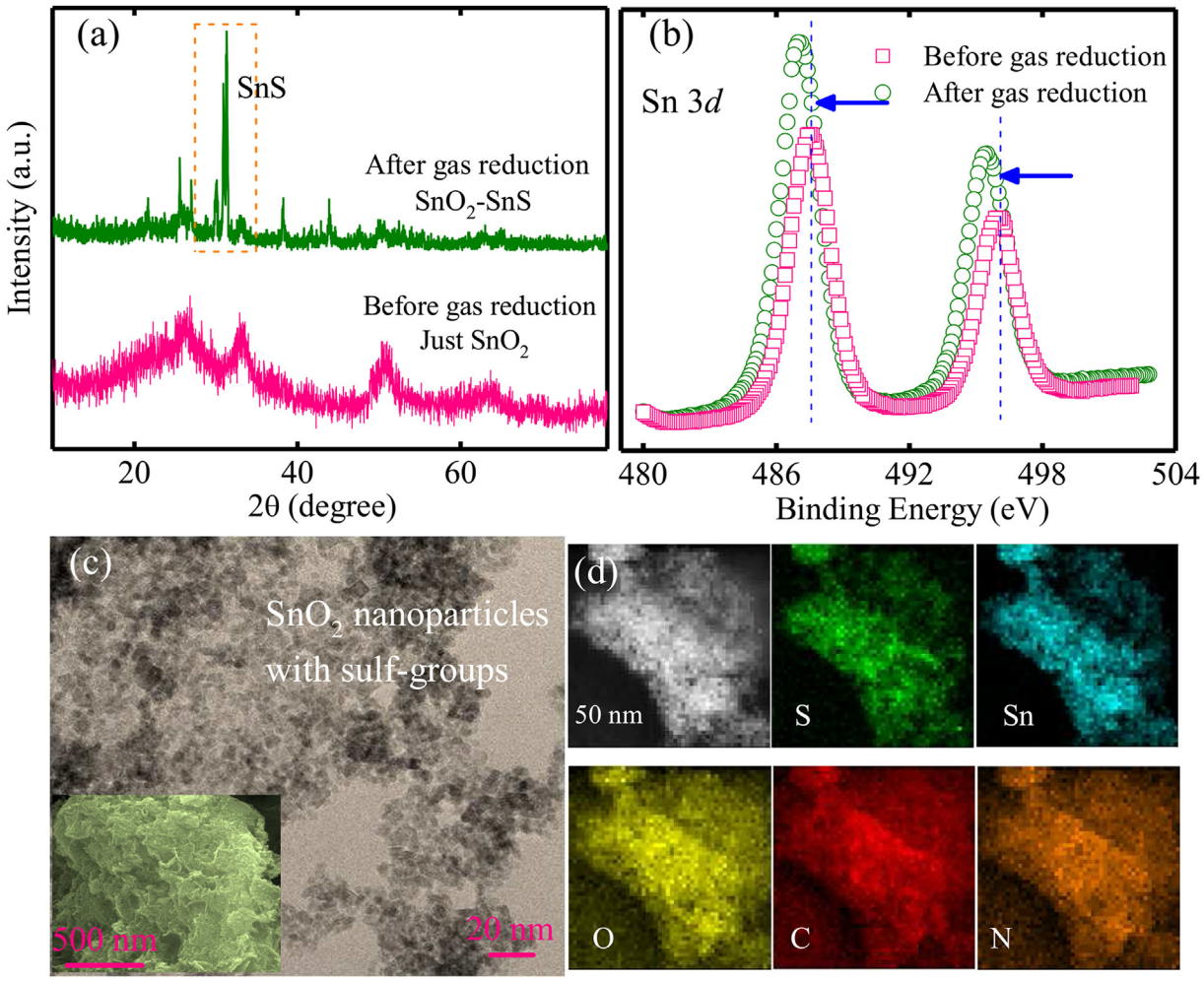

Fig. 4. (a) XRD patterns and (b) The XPS high resolutions for Sn 3d of the precursor before and after gas reduction. (c) TEM image of the precursor before gas reduction and (d) the related element mapping for S, Sn, O, C, and N, respectively.

same as above XPS analysis in SnO_2@Gr and C@SnS-SnO_2@NGr. From this, we could conclude that the hydrothermal and annealing process worked as the pre-sulfuration and reduction effects. In addition, with the addition of GO and before annealing, SEM and TEM-element mapping images have been provided in Fig. 4c and d. Though only SnO_2 diffraction peaks can be observed, the well-distribution of S and N elements are indicative of the N-doped GO and existence of sulfur-groups. The content of sulfur can be further confirmed from the XPS analysis of Pre-S-SnO_2@NGr with the atomic ratio of about 8.35% (Fig. S6), which matches well with the EDS analysis of C@SnS-SnO_2@NGr after gas reduction (Fig. S5). Thus, we can take these as powerful evidence to deduce the H_2S gas reduction process, which ensure a homogeneous and fluffy than conventional hydrothermal methods. Therefore, the induced defect sites, improved conductivity by N-doped GO, and the in-situ gas reduction strategy endow fine SnO_2/SnS nanoparticles and benefit to enhance the charge-transfer kinetics by synergistic effects.

3.4. Electrochemical evaluation and kinetics investigation of LIBs

Fig. 5a shows the cyclic voltammograms (CV) of anodes made with gas reduction C@SnS-SnO_2@NGr to study the electrochemical reactions at a scan rate of 0.5 mV s^{-1} from the voltage 0.02−3 V. During the first cathodic process, two reduction peaks located at 1.44 V and 1.1 V can be corresponding to the decomposition of SnS into Sn and Li_2S (Eq.γ: $SnS + 2Li^+ + 2e^- \leftrightarrow Sn + Li_2S$). According to previous studies, without the phase decomposition, Li^+ could intercalate into SnS layers and form the Li_xSnS firstly [27,28]. An evident peak near 0.77 V could be attributed to the reduction of SnO_2 to Sn Eq(α) and the formation of the solid electrolyte interphase (SEI) layer. Another weak slope at 0.1 V represents the Sn-Li alloying reaction Eq(β). In the following oxidation scan, three peaks at around 0.58 V, 0.68 V, and 0.8 V are attributed to the reversible dealloying of Li_xSn. Then, two broad peaks appear at 1.32 V and 1.91 V, which can be assigned to the partial delithiation of Li_2O and Li_2S. Whereafter, in cathodic cycle, a small peak at 0.62 V is ascribed to the conversion from SnO_2 to Sn, and reduction peak at 1.1 V shifts to 1.25 V, which can act as the evidence for the formation of some infaust productions. Fortunately, after few cycles, it keeps invariable and indicates a stable state of C@SnS-SnO_2@NGr anode. These can be expressed that, first of all, enhanced charge-transfer behaviors in C@SnS-SnO_2@NGr can bring continuous Li^+ insertion and bate the localized reaction of SnM_x. Then, after further alloying process, well-spread fine nanoparticles and superior electric contact can restrain the obvious aggregation and crush of Li_xSn. Afterwards, available contact of Li_xSn and Li_2M provides expected possibility of reversibility of reaction Eq.(α) and (γ) [12]. However, from the CV curve of SnS@Gr (Fig. S7), the corresponding reduction process fade away at 1.22 V due to the inferior ion diffusion kinetics and unavoidable aggregation of SnS nanoparticles. Moreover, the

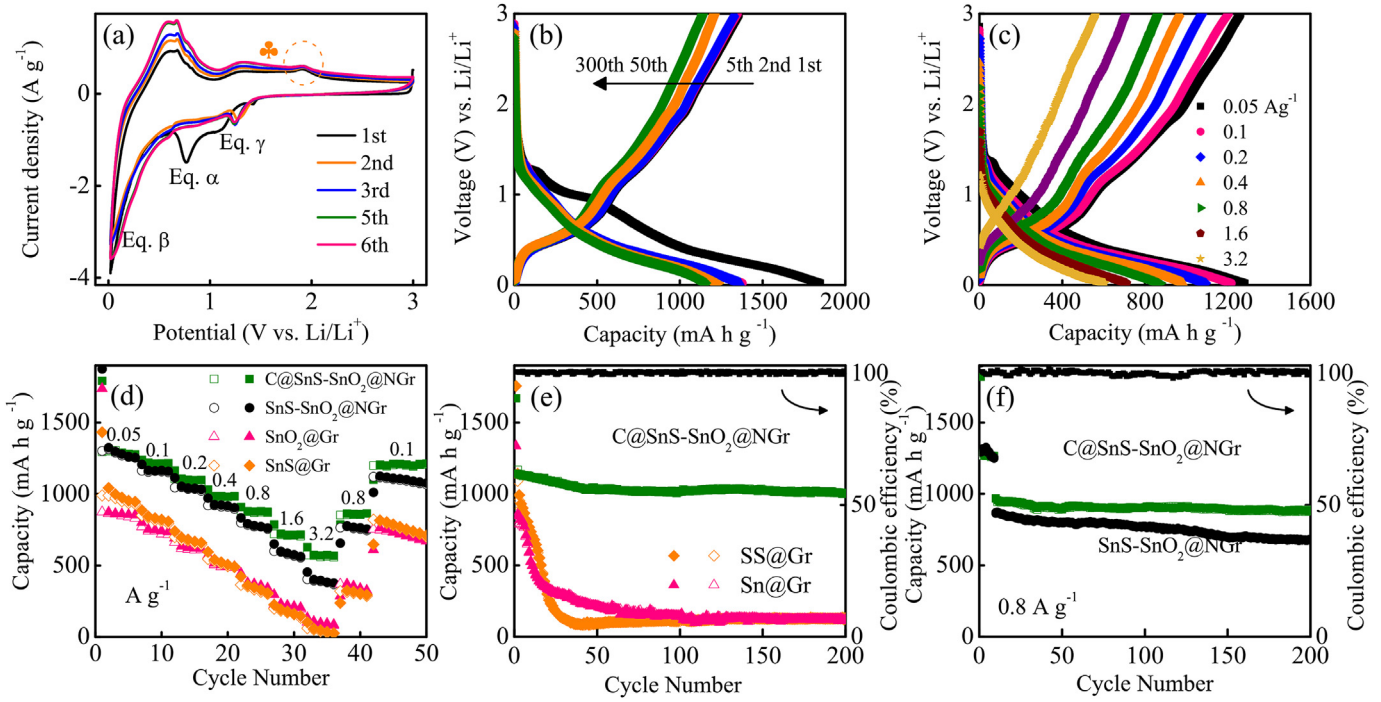

Fig. 5. Electrochemical performances of as-prepared anode electrode. (a) CV curves of C@SnS-SnO_2@NGr for the first six cycles at sweep rate of 0.5 mV s^{-1}. (b) The GDC profiles of C@SnS-SnO_2@NGr for 1st, 2nd, 5th, 50th, and 300th cycles at 0.1 A g^{-1}. (c) The GDC profiles of C@SnS-SnO_2@NGr at increasing discharge current density from 0.05 to 3.2 A g^{-1}. (d) Rate performances of as-assembled batteries. (e) Cycle stability of C@SnS-SnO_2@NGr anode with 2.5 mg cm^{-2} at 0.2 A g^{-1} and other anodes with 0.8 mg cm^{-2} at 0.1 A g^{-1} for 200 cycles. (f) Cycle performances of as-synthesized composites at 0.8 A g^{-1} for 200 cycles.

stabilized delithiation peak at 1.91 V of Li_2S to SnS verified the more invertible in C@SnS-SnO_2@NGr anode, as compared with that of SnS@Gr, which disappeared gradually [44]. Therefore, the increased reversibility and electrochemical properties of the C@SnS-SnO_2@NGr anode are favorable to the high Coulombic efficiency and durability energy storage.

Fig. 5b shows the galvanostatic discharge-charge (GDC) curves (1st, 2nd, 5th, 50th, and 300th) of the electrodes (Fig. S8) at the current density of 0.1 A g^{-1}. In the first discharge profile of C@SnS-SnO_2@NGr anode, there exist two plateau near 1.3 V and 1–0.85 V, which are related to the intercalation of intercalation of Li^+ and the conversion reaction. For SnO_2@Gr, the first discharge and charge capacities were 1360 and 840 mA h g^{-1}, respectively, with an initial Coulombic efficiency of 62%. The inferior reversibility is almost attributed to the nonreversing formation of SEI and Li_2O from SnO_2. Both SnO_2@Gr and SnS@Gr anodes were suffered from rapid capacity decay of 90% within 50 cycles. However, after in-situ gas reduction, the initial Coulombic efficiency increased to 78%, with the first discharge and charge capacities were 1780 and 1380 mA h g^{-1}, respectively. Besides, the high reverse capacity of SnS-SnO_2@NGr anode remained 56% for 500 cycles relative to the second discharge (Fig. S9). Significantly, after vapor polymerization procedure, appreciable capacity retention of 85% for 500 cycles (1120 mA h g^{-1}) reveals the areal and volumetric capacity of about 1.2 mA h cm^{-2} and 1430 mA h cm^{-3}, respectively. Note that the volumetric capacity is more than twice of practical graphite anode (560 mA h cm^{-3}). It intensely indicates the critical role of carbon layer in protecting the inner matrix from mechanical stress and ensuring the electrochemical stability, as well as the paradigm to alloying-anodes for LIBs applications. Accordingly, the C@SnS-SnO_2@NGr composite is composed of 9% carbon/graphene, 33% SnS, and 58% SnO_2, which enables theoretical capacity with about 372, 782, and 782 mA h g^{-1}, respectively. Thus, we could deduce that the experimental capacity of the anodes are higher than the theoretical contribution of SnS/SnO_2 and graphene to the total capacity. Actually, SnO_2 anode is related to two-step reduction/intercalation process (α) and (β) with the theoretical capacity of 711 and 782 mA h g^{-1}, respectively, in which the reduction reaction (α) was generally assumed to be irreversible [16,22,28,47]. While in this present work, the process (α) (the oxidization of Sn to SnO_2) was verified to be highly reversible via the CV curves of C@SnS-SnO_2@NGr anode, which effectively endows a considerable total capacity. In addition, after the gas reduction process, the formation of heterostructure is favorable to the electronic contact, as well as the reversibility of Li_2O and Li_2S [27]. Besides, both the carbon film and the N-doped Gr could provide available active sites and bicontinuous ion pathway for lithiation and delithiation process. In addition, the contribution of pseudocapacitive kinetics are favorable to faster Li^+ intercalation reaction and storage capacity, which would be discussed in detail. As a result, the composites delivers an excellent capacity relying on the above superiorities, which also including the unavoidable errors during weighing and measurement process. In Fig. 5c and d, the rate performance of the four anodes were investigated at high current densities up to 3.2 A g^{-1}. Clearly, C@SnS-SnO_2@NGr material presents a higher capacity and stabilization states than all other anodes. Concretely, at 3.2 A g^{-1} it remains about 570 mA h g^{-1}. Then a reversible capacity about 1200 mA h g^{-1} was achieved when returning the current density to 0.1 A g^{-1}. While, with increasing current density, the capacities of SnO_2@Gr and SnS@Gr anodes fade seriously, from 1030 to 720 mA h g^{-1} and 880 to 660 mA h g^{-1}, respectively. The poor rate behaviors and serious decay are related to the worse electric contact and weak protection from carbon layer. Apart from varying the current density, a higher mass loading of C@SnS-SnO_2@NGr electrode about (2.5 mg cm^{-2}) was also investigated in Fig. 5e. It assuredly exhibits a mild capacity loss at 0.2 A g^{-1}, which is derived from the higher internal resistance and overpotential compared with lighter anodes. Notably, the superior cycling stability was still

manifested with the maintained capacity of 1000 mA h g^{-1} after 200 cycles.

In addition, compared with diminishing capacities of SnS-SnO_2@NGr, C@SnS-SnO_2@NGr anode possesses more integrated protection by the thin carbon layer, which delivers superior capacity of 880 mA h g^{-1} at 800 mA g^{-1} after 200 cycles (Fig. 5f). These rate results forcefully manifest the vital roles of N-doped graphene, uniform gas reduction and fine SnO_2/SnS nanoparticles for Li^+ storage. Interestingly, as shown in Fig. 6b, cyclic voltammetry at scan rates from 0.1 to 1 mV s^{-1} were also measured to investigate the energy storage kinetic behavior of C@SnS-SnO_2@NGr anode. In the CV curves, the cathodic and anodic peaks become wide piecemeal in the potential range of 0.02−3 V. Based on this, the effects of capacitive capacity and diffusion-controlled capacity can be qualitatively obtained. Note that the relation between current (i) and sweep rate (v) can be represented as $i = av^b$, where a and b are appropriate values [5]. For diffusion-controlled process, the value of b is close to 0.5, and for surface capacitance capacity, it approaches 1. From the fitted result in Fig. 6c, the cathodic (0.65 V) and anodic (1.25 V) b values for C@SnS-SnO_2@NGr are about 0.88 and 0.87, respectively. It indicates a mainly pseudocapacitive dominated kinetics, including surface/subsurface redox reactions, and thus reveals the faster Li^+ intercalation reaction and better rate performance. For comparison, the CV curves with varying sweep rates for SnO_2@Gr were conducted (Fig. S10) Evidently, the lower b values reveal the small contribution of capacitance capacitive system in SnO_2@Gr, as well as the worse reaction kinetics. Besides, the enhanced conductivity of anode materials have been studied by the electrochemical impedance spectra (EIS) (Fig. 6d). Through pre-sulfuration and gas reduction, the anodes show a lower initial interfacial resistance and higher charge transfer rate than SnO_2@Gr or SnS@Gr, also it can be ameliorated via carbon layer. Accordingly, using the equivalent circuit (the inset of Fig. 6d), the relative parameter could be fitted from the semicircle in high frequency region of C@SnS-SnO_2@NGr hybrid. The results further indicate its smallest charge transfer resistance (R_{ct}-21 Ω), enhanced charge transfer process and electrolyte accessibility than other electrodes (Fig. S11). In particular, it decreases slightly after cycling for 10 cycles, which are in agreement with the better electrochemical performance and improved charge-transfer kinetics.

To corroborate the durability of C@SnS-SnO_2@NGr hybrids, high rate evaluations at 2.0 A g^{-1} was further conducted for 1000 cycles. As shown in Fig. 6a, it exhibits high electroactivity with 630 mA h g^{-1} remained after 1000 cycles. In contrary, the capacity of SnO_2@Gr electrode suffered serious degradation without the matrix of N-doped graphene or the improved transfer kinetic. Undergoing the high rate GDC, Pre-S-SnO_2@NGr electrode seems to show a similar behavior with SnO_2@Gr due to the dangling sulfurated group outside. It further corroborated the effective gas reduction and the synergistic effects between SnO_2 to SnS. Obviously, the reversible capacity for C@SnS-SnO_2@NGr anode undergoes interesting stages, which seems to be divided into four parts, as quick fading, lower capacity, steady grow up, and durable states, respectively. Firstly, after activated, it delivers an initial capacity of 800 mA h g^{-1}. However, due to the formation of SEI on Sn and Li_2M, active particles tend to pin on the surface of graphene or SEI shell, leading to the quick fading in the initial 50 cycles. Secondly, the electrode keeps stable GDC process in around 300 cycles with lower capacity (350 mA h g^{-1}). Next, during repeated Sn-Li alloying reaction, the Sn particles may shrink in size and acquire a lower activation energy. Thus the third stage allows more reversibility conversion and a growing-up lithium storage until 800 cycles. Then in the last part, the electrode works into steady states, with outstanding capacity of 630 mA h g^{-1} after 1000 cycles, during which few metal lithium might be produced slightly at a high current density (2.0 A g^{-1}) with little contribution to the total capacity [48,49]. To the best of our knowledge, it is almost longest

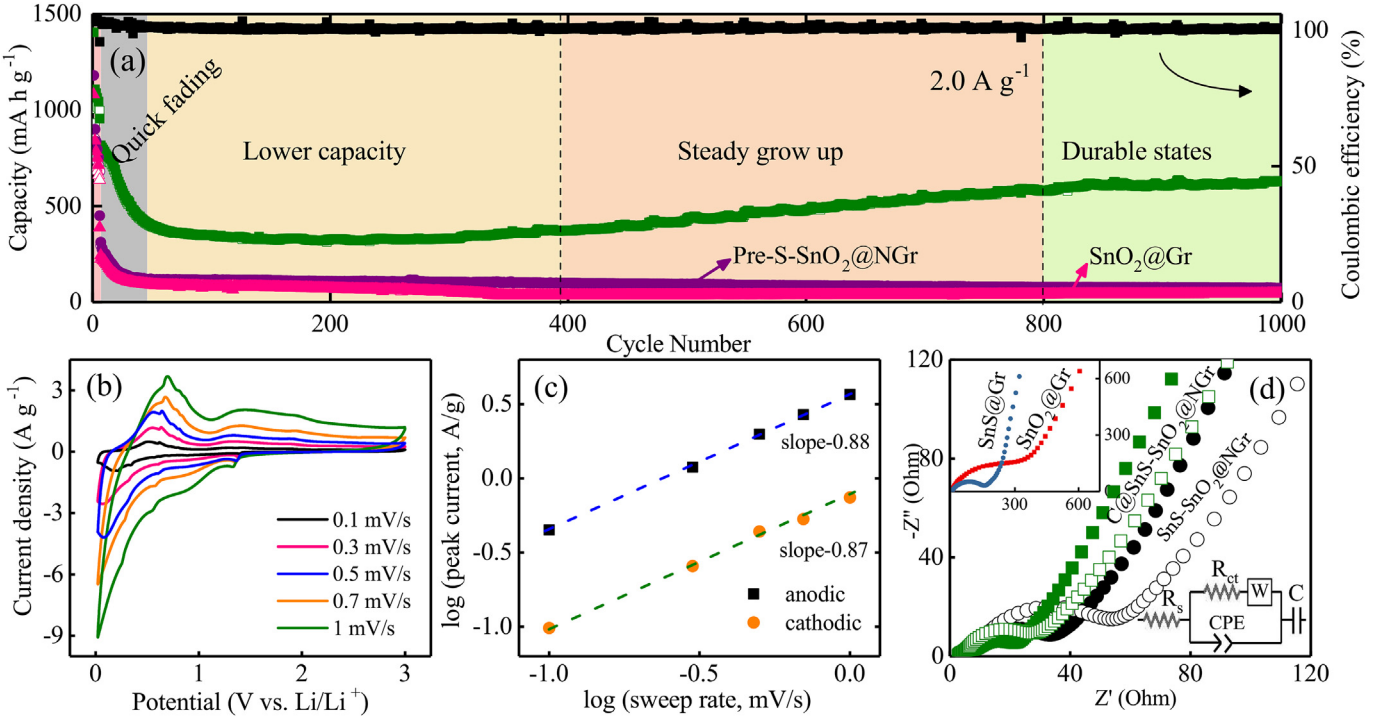

Fig. 6. (a) Durable rate cycling of C@SnS-SnO_2@NGr, Pre-S-SnO_2@NGr and SnO_2@Gr at 2.0 A g^{-1} for 1000 cycles. (b) CV curves and (c) specific peak current at various sweep rates from 0.1 to 1 mV s^{-1}. Note that the dotted lines are the fitted results. (d) The electrochemical impedance spectra (EIS) of as-prepared samples before and after several cycles. Inset shows the equivalent circuit. Note that the vacant and solid dots indicate before and after cycles, respectively.

cycle life of SnO_2-SnS heterostructure anodes as surveyed. The above durable electroactivity is correlated to the uniform anchoring of fine SnO_2-SnS nanoparticles and enhanced conductivity of composites. Moreover, at the current density of 2.0 A g^{-1}, the GDC profiles for 10th, 50th, 400th, 800th, and 1000th cycles (Fig. S12) remain similar characteristic with those in Fig. 5b. While the abridged plateau at lower voltage during high-rate tests also can be observed in other works [28]. It is believed to be ascribed to the dominated surface-controlled capacitive, which is agreement with the results in Fig. 6c.

As a consequence, the conceivable mechanism has been put forward to reveal the superior performance of C@SnS-SnO_2@NGr anodes (Fig. 7a). Based on previous studies, SnO_2 and SnS are n and p-type semiconductors with band gaps of 3.8 and 1.3 eV, respectively [46,50]. Thus, according to the well-matched crystal surface between SnS and SnO_2 (Fig. 7b), there can be introduced an inner electric field at the p-n heterointerface. Firstly, during the discharge process, the transfer and diffusion of Li^+ into SnO_2/SnS could be promoted by electronic force. Then in the charge process, more released Li^+ region at SnS domain would induce a reversed electric field at the heterointerface from SnS to SnO_2 owing to the worse reversibility of Li_2O than Li_2S. Thus, the reversed driving force will facilitate the electron/ion diffusion through fine nanoparticles and avoid the localization of Li_2O, as well as restrains the obvious aggregation of Li_xSn. Therefore, a reversible capacity and remarkable electrochemistry activity can be guaranteed. Correspondingly, compared with summarized previous work (the Table in Fig. 7c), the SnO_2-SnS based heterostructure anodes in present study delivers highest ICE (78%) and best cycle stability and durable rate performance.

For further insight into the evolution of anode materials, the inner-structure after GDC process at 2.0 A g^{-1} has been investigated by prospective in-situ Raman spectra and HRTEM/element mapping analysis. As shown in Fig. 8a, after first discharge, the featured peaks disappeared at around 160–220 cm^{-1} and 500–700 cm^{-1}, indicating the consumption of SnO_2 and SnS. Afterwards, they became reappeared weakly after the next charging, which evidently presents the reversible conversion reaction of the composite anode. In Fig. 8b–c, fine particles are well dispersed on graphene nanosheets, without obvious aggregation. Compared with the particles before GDC cycles and the TEM images of SnO_2@Gr after GDC cycles (Fig. S12), the HRTEM in Fig. 8d presents smaller size particles (7–9 nm in diameter), corresponding to the certain shrink at the initial GDC stages. In the inset of Fig. 8b, the SAED pattern indicates the polycrystalline nature of C@SnS-SnO_2@NGr. Meanwhile, the little reflection spots were recognized as the few Sn nonreversible metal, which verified the almost reversible conversion. However, after the same GDC cycles, the twinkling features of larger Sn particles was detected in the SAED of the worse SnO_2@Gr electrode (Fig. S13). As an evidence, the

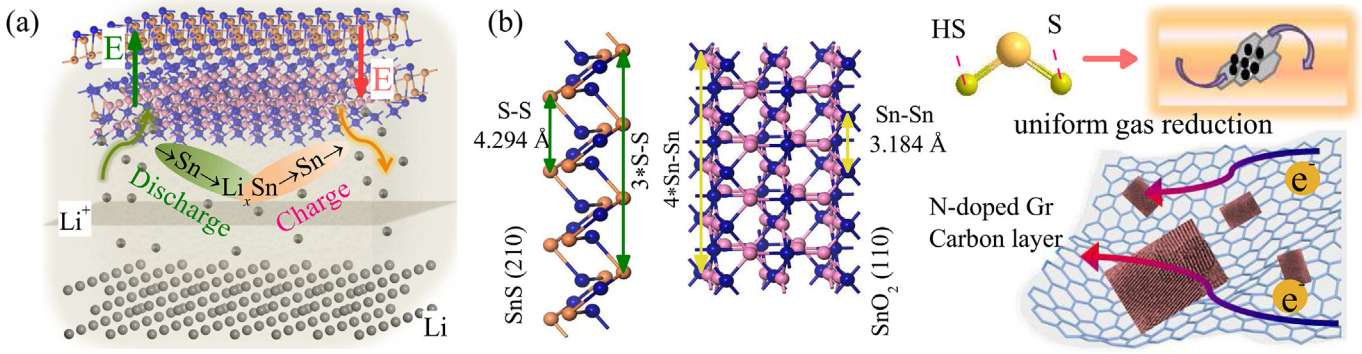

(c)

Anode materials	Reverisible capacity (mA h g^{-1})	Mass loading (mg cm^{-2})	ICE (%)	Cycling stablity/ High rate (mA h g^{-1})	Reference
Porous C-SnO_2 submicrocubes	1220 mA h g^{-1} at 0.05 A g^{-1}	0.3-0.5	41.1%	71.3% at 0.05 A g^{-1} after 120 cycles 516 at 1C after 200 cycles	37
N-doped graphene SnO_2 foams	1262 mA h g^{-1} at 0.05 A g^{-1}	1.6	61.2%	139% at 0.1 A g^{-1} after 200 cycles 1029 at 1 A g^{-1} after 1000 cycles	14
SnS/N-doped graphene	434 mA h g^{-1} at 0.2 A g^{-1}	0.5-0.6	45%	279 at 0.2 A g^{-1} after 100 cycles	27
Carbon@N-doped graphene@SnS-SnO_2	1300 mA h g^{-1} at 0.1 A g^{-1}	–	95%	1236 at 0.1 A g^{-1} after 110 cycles	20
Carbon@SnS-SnO_2 on carbon nanofibers	918 mA h g^{-1} at 0.2 A g^{-1}	–	72.54%	152% at 0.2 A g^{-1} after 200 cycles 827 at 1 A g^{-1} after 500 cycles	43
Carbon sealed gas reduction SnS-SnO_2 on N-doped graphene	1330 mA h g^{-1} at 0.1 A g^{-1}	0.8-1.0	78%	83.5 % at 0.1 A g^{-1} after 500 cycles 880 at 0.8 A g^{-1} after 200 cycles 630 at 2 A g^{-1} after 1000 cycles	This work

Fig. 7. (a) The structure evolutions of the half-cell during charging/discharging and the improved transfer kinetics mechanism of C@SnS-SnO_2@NGr for LIB applications. (b) The cleaved crystal structure of SnS and SnO_2 with (210) and (110) crystal planes, respectively. (c) Table I: The survey of the SnO_2 or SnS-based anodes in the application of Li^+ storage.

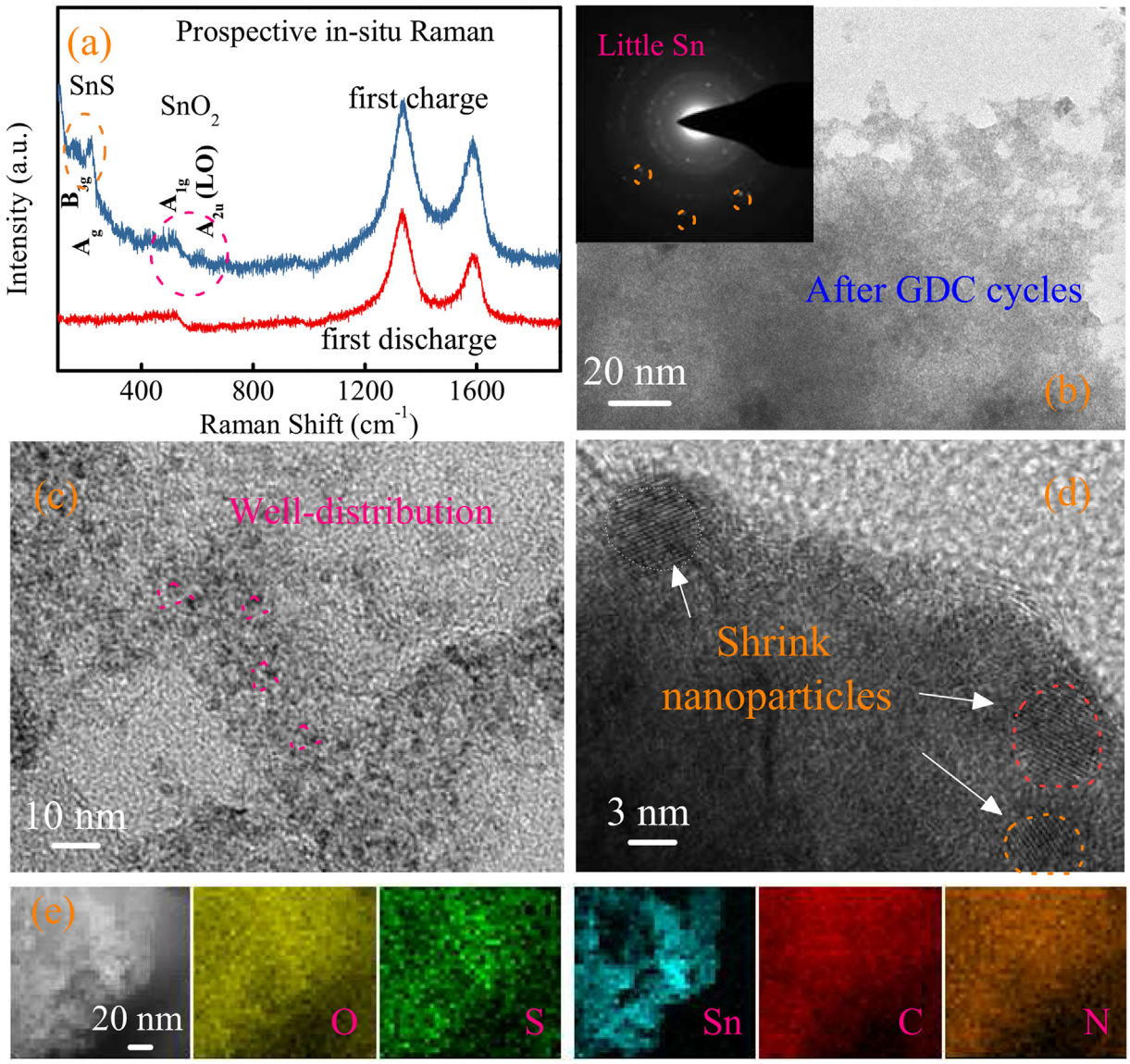

Fig. 8. (a) The Raman spectra of the C@SnS-SnO_2@NGr anodes after first discharge and first charge process. (b)–(d) TEM images and HRTEM analysis of C@SnS-SnO_2@NGr anode materials after GDC cycles at 2.0 A g^{-1}. (e) The corresponding TEM-element mapping for O, S, Sn, C, and N, respectively. The inset of (b) shows the SAED pattern of the cycled electrode.

homogeneous element distribution (Fig. 8e) corroborated the complete N-doped and uniform gas reduction, which is essential to better electric contact, higher Coulombic efficiency, and faint fading. Thus N-doped graphene and carbon layer provide bicontinuous conductive network and short distance of electron transport, which ensure the stable and durable capacitance. Besides, benefitted from the uniform SnO_2-SnS interface, fine-interspersed nanoparticles brought better contact of Li_2O and Sn during cycling, which avoids severe aggregation and pulverization. Generally, the construction of the rigorous conductive network indeed demonstrate the feasible strategy of H_2S gas reduction for SnO_2/SnS heterostructure and offer an available method for next generation of energy storage materials.

4. Conclusion

In summary, different from the universal fabrication of heterostructure, a simple but effective method referring to pre-sulfuration and gas reduction is conducted, aiming to achieve a well distribution of fine SnO_2/SnS nanoparticles on graphene nanosheets for lithium ion storage applications. Based on the uniform composite anode materials, enhanced internal charge-transfer kinetics in heterointerface can promote the ion/electron diffusion and electric contact. During charge/discharge processes, serious localized reaction of Li_2M can be restrained by intimate continuity of fine nanoparticles. Ameliorative aggregation or cracking of Sn/Li_xSn groups brought almost reversible conversion between SnM_x and Sn/Li_2M. In addition, the N-doped graphene and carbon layer framework provide numerous nucleation sites, suitable buffer and bicontinuous conductive channels. As a result, the C@SnS-SnO_2@NGr anode delivers a superior ICE (78%) among most Sn-based anodes and still remains 630 mA h g^{-1} at 2.0 A g^{-1} for 1000 cycles, in which verified the dominated surface-controlled capacitance kinetics. Hence, it further verifies the synergistic effects and improved conductivity of hybrids, meanwhile creates an admissible pre-sulfuration strategy for practical applications.

Acknowledgments

This work was financially supported by National Key Research and Development Program of China (Grants No. 2017YFA0303403 and 2018YFB0406500), the Natural Science Foundation of China (Grant Nos. 61674057, 11374097, 61376129, 61504156, and 61227902), Projects of Science and Technology Commission of Shanghai Municipality, China (Grant Nos. 18JC1412400, 18YF1407200, and 18YF1407000), and the Program for Professor of Special Appointment (Eastern Scholar) at Shanghai Institutions of Higher Learning and the Fundamental Research Funds for the Central Universities.

Appendix A. Supplementary data

Supplementary data related to this article can be found at https://doi.org/10.1016/j.jallcom.2018.08.038.

References

[1] N.-S. Choi, Z. Chen, S.A. Freunberger, X. Ji, Y.-K. Sun, K. Amine, G. Yushin, L.F. Nazar, J. Cho, P.G. Bruce, Challenges facing lithium batteries and electrical double-layer capacitors, Angew. Chem. Int. Ed. 51 (2012) 9994–10024.
[2] G. Zeng, N. Shi, M. Hess, X. Chen, W. Cheng, T. Fan, M.A. Moedernerger, A general method of fabricating flexible spinel-type oxide/reduced graphene oxide nanocomposite aerogels as advanced anodes for lithium-ion batteries, ACS Nano 9 (2015) 4227–4235.
[3] F.M. Hassan, Z. Chen, A. Yu, Z. Chen, X. Xiao, Evidence of covalent synergy in silicon-sulfur-graphene yielding highly efficient and long-life lithion-ion batteries, Nat. Commun. 6 (2015) 8597.
[4] F.M. Hassan, V. Chabot, A.R. Elsayed, X. Xiao, Z. Chen, A scalable post-fabrication treatment for the production of next-generation Li-ion batteries, Nano Lett. 14 (2014) 277–283.
[5] D. Chao, P. Liang, Z. Chen, L. Bai, H. Shen, X. Liu, X. Xia, Y. Zhao, S.V. Savilov, J. Lin, Z.X. Shen, Pseudocapacitive Na-Ion storage boosts high rate and areal capacity of self-branched 2D layered metal chalcogenide nanoarrays, ACS Nano 10 (2016) 10211–10219.
[6] Y. Jiang, M. Wei, J. Feng, Y. Ma, S. Xiong, Enhancing the cyding stability of Na-Ion batteries by bonding SnS_2 ultrafine nanocrystals on amino-functionalized graphene hybrid nanosheets, Energy Environ. Sci. 9 (2016) 1430–1438.
[7] W. Xu, T. Wang, S. Wu, S. Wang, N-doped carbon-coated MoS_2 nanosheets on hollow carbon microspheres for high-performance lithium-ion batteries, J. Alloys Compd. 698 (2017) 68–76.
[8] Y.C. Zhang, Z.N. Du, K.W. Li, M. Zhang, D.D. Dionysiou, High-performance visible-light-driven SnS_2/SnO_2 nanocomposite photocatalyst prepared via in situ hydrothermal oxidation of SnS_2 nanaparticles, ACS Appl. Mater. Interfaces 3 (2011) 1528–1537.
[9] Z.A. Ghazi, X. He, A.M. Khattak, N.A. Khan, B. Liang, A. Lqbal, J.X. Wang, H. Sin, L.S. Li, Z.Y. Tang, MoS_2/Celgard separator as efficient polysulfide barrier for long-life lithium-sulfur batteries, Adv. Mater. (2017) 1606817.
[10] C.L. Tan, X.H. Cao, X.-J. Wu, Q.Y. He, J. Yang, X. Zhang, J.Z. Chen, W. Zhao, S.K. Han, G.-H. Nam, M. Sindoro, H. Zhang, Recent advances in ultrathin two-dimensional nanomaterials, Chem. Rev. 117 (2017) 6225–6331.
[11] X. Zhao, J.H. Sui, F. Li, H.T. Fang, H.G. Wang, J.Y. Li, W. Cai, G.Z. Cao, Lamellar $MoSe_2$ nanosheets embedded with MoO_2 nanoparticles: novel hybrid nanostructures promoted excellent performances for lithium ion batteries, Nanoscale 8 (2016) 17902.
[12] W.J. Dong, J.J. Xu, C. Wang, Y. Lu, X.Y. Liu, X. Wang, X.T. Yuan, Z. Wang, T.Q. Lin, M.L. Sui, I.-W. Chen, F.Q. Huang, A robust and conductive black tin oxide nanostructure makes efficient lithium-ion batteries possible, Adv. Mater. (2017), 1700136.
[13] S.J.R. Prabakar, Y.-H. Hwang, E.-G. Bae, S. Shim, D. Kim, M.S. Lah, K.-S. Sohn, M. Pyo, SnO_2/Graphene composites with self-assembled alternating oxide and amine layers for high Li-Storage and excellent stability, Adv. Mater. 25 (2013) 3307.
[14] J.Y. Huang, L. Zhong, C.M. Wang, J.P. Sullivan, W. Xu, L.Q. Zhang, S.X. Mao, N.S. Hudak, X.H. Liu, A. Subramanian, H. Fan, L. Qi, A. Kushima, J. Li, In situ observation of the electrochemical lithiation of a single SnO_2 nanowire electrode, Science 330 (2010) 1515.
[15] A.S. Hassan, K. Moyer, B.R. Ramachandran, C.D. Wick, Comparision of storage mechanisms in RuO_2, SnO_2, and SnS_2 for lithium-ion battery anode materials, J. Phys. Chem. C 120 (2016) 2036–2046.
[16] H.P. Cong, S. Xin, S.H. Yu, Flexible nitrogen-doped graphene/SnO_2 foams promise kinetically stable lithium storage, Nano Energy 13 (2015) 482.
[17] Z.Y. Wang, D.Y. Luan, F.Y.C. Boey, X.W. Lou, Fast formation of SnO_2 nanoboxes with enhanced lithium storage capability, J. Am. Chem. Soc. 133 (2013) 4738–4741.
[18] H. Gao, T.F. Zhou, Y. Zheng, Y.Q. Liu, J. Chen, H.K. Liu, Z.P. Guo, Integrated carbon/red phosphorus/graphene aerogel 3D architecture via advanced vapor-redistribution for high-energy sodium-ion batteries, Adv. Energy Mater. (2016), 1601037.
[19] F.M. Hassan, A.R. Elsayed, V. Chabot, R. Batmaz, X. Xiao, Z. Chen, Subeutectic growth of Single-Crustal silicon nanowires grown on and wrapped with graphene nanosheets: high-performance anode material for lithium-ion battery, ACS Appl. Mater. Interfaces 6 (2014) 13757–13764.
[20] Q.G. Shao, J. Tang, Y.G. Sun, J. Li, K. Zhang, J.S. Yuan, D.-M. Zhu, L.-C. Qin, Unique interconnected graphene/SnO_2 nanoparticle spherical multilayers for lithium-ion battery applications, Nanoscale 9 (2017) 4439.
[21] B.B. Jiang, Y.J. He, B. Li, S.Q. Zhao, S. Wang, Y.-B. He, Z.Q. Lin, Nitrogen-doped carbon-encapsulated SnO_2-SnS/graphene sheets with improved anodic performance in lithium ion batteries, Angew. Chem. Int. Ed. 56 (2017) 1–5.
[22] Y.Q. Zhang, Z.L. Ma, D.D. Liu, S. Dou, J.M. Ma, M. Zhang, Z.P. Guo, R. Chen, S.Y. Wang, p-Type SnO thin layers on n-type SnS_2 nanosheets with enriched surface defects and embedded charge transfer for lithium ion batteries, J. Mater. Chem. A 5 (2017) 512.
[23] M.J. Li, J.Y. Wang, P. Zhang, Q.L. Deng, J.Z. Zhang, K. Jiang, Z.G. Hu, J.H. Chu, Superior adsorption and photoinduced carries transfer behaviors of dandelion-shaped Bi_2S_3@MoS_2: experiments and theory, Sci. Rep. 7 (2017) 42484.
[24] Y. Zheng, T.F. Zhou, C.F. Zhang, J.F. Mao, H.K. Liu, Z.P. Guo, Boosted charge transfer in SnS/SnO_2 heterostructure: toward high rate capability for sodium-ion batteries, Angew. Chem. Int. Ed. 55 (2016) 3408–3413.
[25] Y. Liu, Y. Jiao, B. Yin, S.W. Zhang, F.Y. Qu, X. Wu, Enhanced electrochemical performance of hybrid SnO_2@MO_x (M=Ni, Co, Mn) core-shell nanostructure grown on flexible carbon fibers as the supercapacitor electrode materials, J. Mater. Chem. A 3 (2015) 3676.
[26] M.-H. Doan, Y. Jin, S. Adhikari, S. Lee, J. Zhao, S.C. Lim, Y.H. Lee, Charge Transport in MoS_2/WSe_2 van der Waals heterostructure with tunable inversion layer, ACS Nano 11 (2017) 3832–3840.
[27] B. Zhao, Z.X. Wang, F. Chen, Y.Q. Yang, Y. Gao, L. Chen, Z. Jiao, L.L. Cheng, Y. Jiang, Three-dimensional interconnected spherical graphene framework/SnS nanocomposite for anode material with superior lithium storage performance: complete reversibilituy of Li_2S, ACS Appl. Mater. Interfaces 9 (2017) 1407–1415.
[28] D.H. Youn, S.K. Stauffer, P.H. Xiao, H. Park, Y. Nam, A. Dolocan, G. Henkelman, A. Heller, C.B. Mullins, Simple synthesis of nanocrystalline tin sulfide/N-doped reduced graphene oxide composites as lithium ion battery anodes, ACS Nano 10 (2016) 10778–10788.
[29] C. Zhu, P. Kopold, W. Li, P. Aken, J. Maier, Y. Yu, A general strategy to fabricate carbon coated 3D porous interconnected metal sulfides: case study of SnS/C nanocomposite for high performance lithium and sodium ion batteries, Adv. Sci. 2 (2015), 1500200.
[30] Y. Denis, P. Prikhodchenko, C. Mason, S. Batabyal, J. Gun, S. Sladkevich, A. Medvedev, O. Lev, High-capacity antimony sulphide nanoparticle-decorated graphene composite as anode for sodium-ion batteries, Nat. Commun. 4 (2013) 2922.
[31] L. Yin, S. Chai, J. Ma, J. Huang, X. Kong, P. Bai, Y. Liu, Effects of binders on electrochemical properties of the SnS_2 nanostructured anode of the lithium-ion batteries, J. Alloys Compd. 698 (2017) 828–834.
[32] J.Q. Shan, Y.X. Liu, P. Liu, Y.S. Huang, Y.Z. Su, D.Q. Wu, X.L. Feng, Nitrogen-doped carbon-encapsulated SnO_2-SnS/graphene sheets with improved anodic performance in lithium ion batteries, J. Mater. Chem. A 3 (2015) 24148.
[33] J. Xia, D.D. Zhu, X.Z. Li, L. Wang, L.F. Tian, J. Li, J.Y. Wang, X. Huang, X.-M. Meng, Epitaxy of layered orthorhombic SnS-$SnS_xSe_{(1-x)}$ core-shell heterostructure with anisotropic photoreponse, Adv. Funct. Mater. 26 (2016) 4673–4679.
[34] L.P. Zhu, L.F. Wang, F. Xue, L.B. Chen, J.Q. Fu, X.L. Feng, T.F. Li, Z.L. Wang, Piezo-phototronic effect enhanced flexible solar cells based on n-ZnO/p-SnS core-shell nanowire array, Adv. Sci. 4 (2017) 1600185.
[35] Z.Y. Jia, S.L. Li, J.Y. Xiang, F.S. Wen, X. Bao, S.H. Feng, R.L. Yang, Z.Y. Liu, Highly sensitive and fast monolayer WS_2 phototransistors realized by SnS nanosheet decoration, Nanoscale 9 (2017) 1916.
[36] W.S. Hummers, R.E. Offerman, Preparation of graphitic oxide, J. Am. Chem. Soc. 80 (1958) 1339.
[37] J.J. Cai, Z.S. Li, P.K. Shen, Porous SnS nanorods/carbon hybrid materials as highly stable and high capacity anode for Li-Ion batteries, ACS Appl. Mater. Interfaces 4 (2012) 4093–4098.
[38] X.F. Du, T.J. Yang, J. Lin, T.Y. Feng, J.B. Zhu, L. Lu, Y.L. Xu, J.P. Wang, Microwave-assisted synthesis of SnO_2@polypyrrole nanotubes and their pyrolyzed composite as anode for lithium-ion batteries, ACS Appl. Mater. Interfaces 8 (2016) 15598–15606.
[39] Z. Mutlu, R.J. Wu, D. Wichramaratne, S. Shahrezaei, C. Liu, S. Temiz, A. Patalano, M. Ozkan, R.K. Lake, K.A. Mkhoyan, C.S. Ozkan, Phase engineering of 2D tin sulfides, Small 22 (2016) 2998–3004.
[40] B. Huang, X.H. Li, Y. Pei, S. Li, X. Cao, R.C. Massé, G.Z. Cao, Novel carbon-encapsulated porous SnO_2 anode for lithium-ion batteries with much improved cyclic stability, Small 14 (2016) 1945–1955.
[41] A.D. Kergommeaux, M. Lopez-Haro, S. Pouget, J.-M. Zuo, C. Lebrun, F. Chandezon, D. Aldakov, P. Reiss, Synthesis, internal structure, and formation mechanism of monodisperse tin sulfide nanoplatelets, J. Am. Chem. Soc. 137 (2015) 9943–9952.
[42] Y. Liu, Y. Jiao, Z.L. Zhang, F.Y. Qu, A. Umar, X. Wu, Hierarchical SnO_2 nanostructures made of intermingled ultrathin nanosheets for environmental remediation, smart gas sensor, and supercapacitor applications, ACS Appl. Mater. Interfaces 6 (2014) 2174–2184.

[43] J. Liu, M.Z. Gu, L.Z. Ouyang, H. Wang, L.C. Yang, M. Zhu, Sandwich-like SnS/polypyrrole ultrathin nanosheets as high-performance anode materials for Li-Ion batteries, ACS Appl. Mater. Interfaces 8 (2016) 8502–8510.
[44] F.M. Hassan, Q.Q. Hu, J. Fu, R. Batmaz, J.D. Li, A.P. Yu, X.C. Xiao, Z.W. Chen, Hot-chemistry structural phase transformation in single-crysta chalcogenides for long-life lithium ion batteries, ACS Appl. Mater. Interfaces 9 (2017) 20603–20612.
[45] S.H. Choi, Y.N. Ko, J.-K. Lee, Y.C. Kang, 3D MoS_2-graphene microsphernes consisting of multiple nanospheres with superior sodium ion storage properties, Adv. Funct. Mater. 25 (2015) 1780–1788.
[46] Q.W. Lian, G. Zhou, X.H. Zeng, C. Wu, Y.H. Wei, C. Cui, W.F. Wei, L.B. Chen, C.C. Li, Carbon coated SnS/SnO_2 heterostructures wrapping on CNFs as an improved-performance anode for Li-Ion batteries: lithiation-induced structural optimazation upon cycling, ACS Appl. Mater. Interfaces 8 (2016) 30256–30263.
[47] Y. Tang, D. Wu, S. Chen, F. Zhang, J. Jia, X. Feng, Highly reversible and ultra-fast lithium storage in mesoporous graphene-based TiO_2/SnO_2 hybrid nanosheets, Energy Environ. Sci. 6 (2013) 2447–2451.
[48] I.W. Seong, C.H. Hong, B.K. Kim, W.Y. Yoon, The effects of current density and amount of discharge on dendrite formation in the lithium powder anode electrode, J. Power Sources 178 (2008) 769–773.
[49] R. Zhang, X.B. Cheng, C.Z. Zhao, H.J. Peng, J.L. Shi, J.Q. Huang, J.F. Wang, F. Wei, Q. Zhang, Conductive Nanostructured scaffolds render Low local current density to Inhibit Lithium dendrite growth, Adv. Funct. Mater. 28 (2016) 2155–2162.
[50] J.J.M. Vequizo, M. Ichimura, Fabrication of electrodeposited SnS/SnO_2 heterojunction solar cells, Jpn. J. Appl. Phys. 5 (2012), 10NC38.